






Signatures of Magnetic Reconnection at the Footpoints of Fan-shaped Jets on a Light Bridge Driven by Photospheric Convective Motions

Xianyong Bai^{1,2}, Hector Socas-Navarro^{3,4} , Daniel Nóbrega-Siverio^{5,6} , Jiangtao Su^{1,2}, Yuanyong Deng^{1,2}, Dong Li^{7,8} , Wenda Cao⁹, and Kaifan Ji¹⁰

¹ Key Laboratory of Solar Activity, National Astronomical Observatories, Chinese Academy of Sciences, 20 Datun Road, Beijing 100012, People's Republic of China; xybai@bao.ac.cn

² School of Astronomy and Space Science, University of Chinese Academy of Sciences, No. 19(A) Yuquan Road, Beijing 100049, People's Republic of China

³ Instituto de Astrofísica de Canarias, Vía Láctea, s/n, E-38205 La Laguna (Tenerife), Spain

⁴ Department of Astrophysics, Universidad de La Laguna, E-38200 La Laguna (Tenerife), Spain

⁵ Institute of Theoretical Astrophysics, University of Oslo, P.O. Box 1029 Blindern, NO-0315 Oslo, Norway

⁶ Rosseland Centre for Solar Physics, University of Oslo, P.O. Box 1029 Blindern, NO-0315 Oslo, Norway

⁷ Purple Mountain Observatory, Chinese Academy of Sciences, No. 8 Yuanhua Road, Qixia District, Nanjing 210034, People's Republic of China

⁸ Key Laboratory of Dark Matter and Space Astronomy, Purple Mountain Observatory, CAS, Nanjing 210034, People's Republic of China

⁹ Big Bear Solar Observatory, New Jersey Institute of Technology, Big Bear City, CA 92314-9672, USA

¹⁰ Yunnan Observatories, Chinese Academy of Sciences, P.O. Box 110, Kunming 650011, Yunnan, People's Republic of China

Received 2018 September 30; revised 2018 October 28; accepted 2018 November 5; published 2019 January 11

Abstract

Dynamical jets are generally found on light bridges (LBs), which are key to studying sunspot decay. So far, their formation mechanism is not fully understood. In this paper, we used state-of-the-art observations from the Goode Solar Telescope, the Interface Region Imaging Spectrograph, the Spectro-polarimeter on board Hinode, and the Atmospheric Imaging Assembly (AIA) on board the *Solar Dynamics Observatory* to analyze the fan-shaped jets on LBs in detail. A continuous upward motion of the jets in the ascending phase is found from the $H\alpha$ velocity that lasts for 12 minutes and is associated with the $H\alpha$ line wing enhancements. Two mini jets appear on the bright fronts of the fan-shaped jets visible in the AIA 171 and 193 Å channels, with a time interval as short as 1 minute. Two kinds of small-scale convective motions are identified in the photospheric images, along with the $H\alpha$ line wing enhancements. One seems to be associated with the formation of a new convection cell, and the other manifests as the motion of a dark lane passing through the convection cell. The finding of three-lobe Stokes V profiles and their inversion with the NICOLE code indicate that there are magnetic field lines with opposite polarities in LBs. From the $H\alpha -0.8$ Å images, we found ribbon-like brightenings propagating along the LBs, possibly indicating slipping reconnection. Our observation supports the idea that the fan-shaped jets under study are caused by magnetic reconnection, and photospheric convective motions play an important role in triggering the magnetic reconnection.

Key words: methods: observational – Sun: activity – Sun: atmosphere – Sun: magnetic fields – sunspots

Supporting material: animations

1. Introduction

Light bridges (LBs), which commonly occur during the sunspot decay phase, are bright and elongated structures that separate umbra cores or are embedded in the umbra. Studying the magnetic and dynamical properties of LBs is very helpful in understanding sunspot decay. According to the brightness and size of LBs, they can be categorized into three types: faint, strong, and granular LBs. Faint LBs have an elongated structure composed of grains with size and shape similar to umbral dots (Sobotka et al. 1993; Sobotka & Puschmann 2009). Strong LBs, whose typical brightness is comparable to the penumbra, separate the umbra into two regions with the same polarity (Rimmele 2008; Rezaei et al. 2012). Granular LBs show convection cells similar to the granules in the quiet Sun (Vazquez 1973; Sobotka et al. 1994; Leka 1997; Rouppe van der Voort et al. 2010).

From observations, it has been found that all LBs have a relatively weaker magnetic field strength and an increased

magnetic inclination compared with the surrounding umbra (Leka 1997; Jurčák et al. 2006; Katsukawa et al. 2007), forming a cusp-like magnetic field configuration at higher layers. Due to the magnetic shear between the horizontal fields of LBs and the vertical fields of umbra, a sharp and strong current layer forms at the edges of the LBs, which is a favorable site for magnetic reconnection (Shimizu et al. 2009; Liu & Liu 2015; Toriumi et al. 2015b). From the line-of-sight (LOS) velocity images, central hot upflows are found in LBs surrounded by cooler fast downflows, sometimes at supersonic speeds (Rimmele 1997; Louis et al. 2009; Lagg et al. 2014; Felipe et al. 2016; Schlichenmaier et al. 2016), supporting their convective origin. In addition, Toriumi et al. (2015b) discovered some small-scale, short-lived convection cells superimposed on the large-scale, long-term velocity structures in the LBs in the formation phase of an active region (AR). Some faint, divergent magnetic patterns are also found, which suggest a continuous supply of weak magnetic flux from the solar interior, transported by large-scale upflows of the LBs (Louis et al. 2015). Felipe et al. (2016) showed that the value of plasma β in LBs is in the range of 1 to 200, indicating that the LBs are dominated by plasma motions.



Original content from this work may be used under the terms of the [Creative Commons Attribution 3.0 licence](https://creativecommons.org/licenses/by/3.0/). Any further distribution of this work must maintain attribution to the author(s) and the title of the work, journal citation and DOI.

In the upper atmosphere on LBs, many dynamical activities are found, which comprise multitemperature and multidisciplinary structures (Rezaei 2018). For example, brightenings are very common on broadband images in the wavelengths Ca II H, AIA 1600, 1700 Å, IRIS 1300, 1400 Å, and Mg II 2796 Å (Berger & Berdyugina 2003; Shimizu et al. 2009; Rezaei 2018). Also, there are lots of long-lasting and recurring jets (or surges) that are seen with the cool chromospheric lines, such as the H α and Ca II lines (Roy 1973; Asai et al. 2001; Bharti et al. 2007; Liu 2012; Louis et al. 2014; Robustini et al. 2016; Song et al. 2017). Bharti (2015) and Yang et al. (2015) reported that most of the jets seen in the chromospheric images show decreasing brightness with height, while they show a bright front in the IRIS 1330 Å slit-jaw images (SJI). Some of the bright fronts also exist in the AIA 171 and 131 Å channels, suggesting that the jets can be heated up to transition-region (TR) and low coronal temperatures (Hou et al. 2016b; Yang et al. 2016; Yuan & Walsh 2016). Moreover, the jets' bright fronts seen in IRIS 1400 Å on LBs are disturbed by their surrounding activities, such as adjacent brightenings and solar flares (Hou et al. 2016a; Felipe et al. 2017; Yang et al. 2017).

Two mechanisms for the formation of jets on LBs are generally supported by observations. One is driven by magnetic reconnection, evidenced by the high speeds (100 km s^{-1}) of the jets and current layers at the edge of the LBs (Toriumi et al. 2015a, 2015b). The other is caused by shocked p-mode waves leaked from the underlying photosphere, with lower speeds and a nearly stationary oscillating period of several minutes (Yang et al. 2015; Hou et al. 2017; Zhang et al. 2017). Tian et al. (2018) show that the jets (or surges) on LBs have two components according to their occurrence frequency and maximum length. The ever-present short surges seem to be related to the upward leakage of magnetoacoustic waves from the photosphere, while the occasionally occurring long and fast surges are obviously caused by the intermittent reconnection. All of the above-mentioned observations reveal the highly dynamical nature of the LBs and their complex interaction with the adjacent environments.

From the theoretical perspective, radiative magnetohydrodynamics (MHD) simulations show their advantage in understanding the detailed physical processes behind the various dynamical events on LBs. Cheung et al. (2010) highlighted the common magnetoconvective origin of LBs, umbral dots, and penumbral filaments during the formation of an AR. Based on the work by Cheung et al. (2010), Toriumi et al. (2015a) found that LBs take root deep down in the convection zone and have a large-scale convective upflow, which is consistent with the observations. The upflow carries part of the weak horizontal fields in deeper layers to the solar surface. Due to the radiative cooling, the ascending plasma loses buoyancy and turns back into the convection zone at the edge of LB lanes, showing downflows. At the LBs' boundaries, a strong electric current layer is formed, providing the energy for various dynamical events. Even though the numerical experiments have been helpful in providing theoretical support for the observations and understanding some key features of LBs, there are no radiative MHD simulations of the jets in the upper layers of LBs.

Some questions are still unresolved about the dynamical jets on LBs, in particular for the occasionally occurring long and fast jets. If they are caused by magnetic reconnection, then what is the trigger mechanism for the reconnection? Could we

obtain more information during the magnetic reconnection? What is the relationship between the dynamical jets and their underlying photospheric evolution of mass flows and magnetic fields? Thanks to high-resolution coordinated observations from ground and space, we are in an advantageous position to answer those open questions.

In this paper, we focus on the fan-shaped jets on LBs that are generally found in the H α off-band images. Similar jets are reported by Asai et al. (2001) and Robustini et al. (2016). The aims are to reveal the fine structures of the photospheric convection on LBs and to find the relationship among the small-scale photospheric flow, brightenings, and the jet-like activities on their upper layers, which helps us understand the coupling between mass and energy on LBs. To that end, we have used joint observations from the Goode Solar Telescope (GST, previously called the New Solar Telescope; Cao et al. 2010), the Interface Region Imaging Spectrograph (IRIS; De Pontieu et al. 2014), the Spectro-polarimeter (SP) instrument on board Hinode (Lites et al. 2013), and the Atmospheric Imaging Assembly (AIA) instrument on board the *Solar Dynamics Observatory* (SDO; Lemen et al. 2012). This way, we have been able to cover the different layers of the solar atmosphere, namely, the photosphere, chromosphere, TR, and corona.

The paper is organized as follows. In Section 2, the data from both ground- and space-based solar telescopes and the way to reduce them are presented. Section 3 shows the results, followed by a summary in the last section (Section 4).

2. Observations and Data Reduction

We have used coordinated observations of GST, IRIS, and HINODE/SP obtained on 2014 August 1 from 17:15 to 17:55 UT. The pointer was centered at heliocentric coordinates $(x, y) = (-192'', -210'')$, targeting the decaying sunspot of AR 12127. The GST data contain simultaneous observations of the photosphere, using the titanium oxide (TiO) line taken with the Broadband Filter Imager, and the chromosphere, using the H α 6563 Å line obtained with the Visible Imaging Spectrometer (VIS). The passband of the TiO filter is 10 Å, centered at 7057 Å, while its temporal resolution is about 15 s with a pixel scale of $0''.0343$. Concerning VIS, a combination of 5 Å interference filter and a Fabry-Pérot etalon is used to get a bandpass of 0.07 Å at the H α line. Its field of view (FOV) is about $70''$ with a pixel scale of $0''.0323$. To obtain more spectral information, we scan the H α line at 11 positions with a 0.2 Å step following this sequence: $\pm 1.0, \pm 0.8, \pm 0.6, \pm 0.4, \pm 0.2, 0.0$ Å. The time used in each scan is 23 s. Both high-order adaptive optics (Cao et al. 2010) and a speckle reconstruction postprocessing method (KISIP speckle reconstruction code; Wöger & von der Lühe 2007) are employed to achieve diffraction-limited resolution images.

IRIS data are taken in a very large, coarse 64-step raster mode, with a step size of $0''.35$, step cadence of 31.8 s, and a raster cadence of 2036 s. The exposure time at each step is 29 s. Several strong emission lines are recorded, such as Si IV 1402.77 Å, Si IV 1393.7 Å, C II 1334.53 Å, and Mg II k 2796.35 Å. The cadences of the SJI in the passbands of 1400, 2796, and 2832 Å are all 112 s. The spatial resolution is about $0''.33$, and the FOV is $22''.4 \times 175''$ and $175'' \times 175''$ corresponding to the 64-step raster mode and the SJI. All of the spectra and images used in the analysis are level 2 data,

including dark current subtraction and flat-field and geometrical corrections (De Pontieu et al. 2014; Tian et al. 2014).

Hinode/SP data are acquired in a fast mode with an FOV of $81'' \times 81''$, a step size of $0''.297$, and a raster cadence of 1080 s. Additionally, in order to analyze the corona response to our event, we have used *SDO* data, including the EUV and UV passbands from the AIA (Lemen et al. 2012) with cadences of 12 s and 24 s, respectively.

The spatial register between the GST and *SDO* is first done by coaligning the AIA 1600 Å images with the GST/TiO data, and then coaligning the TiO data with the H α images at different wavelength positions. We use the AIA 1600 Å, IRIS 2832 Å, and SP continuum images to align the *SDO*, IRIS, and SP data. The uncertainty of the coalignment is about one AIA pixel ($0''.6$). Figure 1 contains the context image of the LBs and fan-shaped jets on the sunspot of AR 12127 that we analyze in the subsequent section. The figure shows data from GST, IRIS, and *SDO*/AIA after the alignment process.

3. Analysis and Results

3.1. Relationship between H α Brightenings at the Footpoints of Fan-shaped Jets and Their Bright Fronts Shown in the AIA EUV Channels

The fan-shaped jets on the LB can be found in the region R1 in Figures 1(b) and (c), corresponding to the velocity derived from the H α line using 11 points and the IRIS SJI in the 1400 Å passband, respectively. The blue and red colors in the LOS velocity images indicate the plasma is showing upward and downward motions on the fan-shaped jets at a relatively cool temperature (less than 10,000 K). The associated online animation clearly reveals this evolution of upflow and downflows. Signatures of the fan-shaped jets can also be identified in the IRIS 1400 Å passband and the six EUV channels of AIA (94, 131, 171, 193, 211, and 335 Å), indicating that they have hot materials, covering from 10^5 to 10^6 K. The cool and hot components seen from the simultaneous multiwavelength observation reveal the multithermal nature of the fan-shaped jets. Moreover, the jets' fronts show brightenings (the region marked by the arrow in Figures 1(d)–(i)) in the above-mentioned passbands, while the footpoint of the jets on the LB has some transient brightenings, especially in the IRIS 1400 Å image.

Along the trajectory of the jets, a slice, labeled as L1, is selected to study the dynamical response of the different solar atmosphere layers to the jets. The corresponding spacetime diagram is presented in Figure 2. The first thing we notice is that the jets follow a parabolic trajectory. This is evident when following the shape of the brightenings (or bright fronts) observed in the six EUV channels of AIA (Figure 2, panels a to f), for example, from 17:27 to 17:36 UT. Evolution of the LOS velocity in the H α line in Figure 2(g) reveals that the jets have blueshifted (upward motion) at the beginning, and then they gradually become redshifted (downward motion) later. Combining with the parabolic trajectory in the plane of the sky (POS), one can imagine that the jets leave the solar surface with a high initial speed, decrease their velocity due to gravity, reach their maximum height, and finally fall back to the solar surface again. The maximum speeds in the LOS and POS directions at the beginning of the jet's eruption are about 25 and 15 km s $^{-1}$ near 17:27 UT. The corresponding values near 17:43 UT are about 30 km s $^{-1}$ each. The two times are selected because line wing enhancements

in the H α line are found in the meantime. The total speeds (square root of the summation of LOS velocity squared and POS velocity squared) of the launched jets at the two times are about 29 and 42 km s $^{-1}$, which are much larger than the typical local sound speed in the chromosphere (less than 10 km s $^{-1}$). The large initial velocity values are likely to promote shock waves, so the bright fronts visible in IRIS and *SDO* can be interpreted as the effect of shock compression of TRs and coronal material as the cool jet slams into it (Robustini et al. 2016). The fast nature of shocks can also produce departures from statistical equilibrium in the different populations of the emitting ions. Therefore, enhanced brightenings in the bright front of the jets could also be related to nonequilibrium effects as they occur in surges due to the quick action of entropy sources (Nóbrega-Siverio et al. 2018).

Figure 2(h) shows temporal sequences of the H α spectrum of VIS at the location marked by the dashed line in Figure 2(g). Both wings of the H α spectrum are extremely enhanced near 17:24 and 17:47 UT, while the line core remains unperturbed, similar to the profiles of Ellerman bombs (EBs; Ellerman 1917; Robustini et al. 2016; Chen et al. 2017; Hong et al. 2017a, 2017b; Song et al. 2017). Generally, the appearance of EB spectra indicates that magnetic reconnection is happening in the upper photosphere or the lower chromosphere, namely near the temperature minimum region. Comparing Figure 2(h) with Figure 2(g), one can find that the line wing's enhancements in the H α spectrum are associated with the blueshift as shown in the LOS velocity, especially near 17:47 UT. At the same time, all of the EUV channels also show brightenings. The velocities found in the jets, together with the enhancements of the wings in the H α spectrum, seem to indicate that the fan-shaped jets studied in this paper are caused by magnetic reconnection.

It is worth mentioning that the LOS velocity in the H α line (Figure 2, panel g) shows a continuous blueshift from 17:42 to 17:54 UT, lasting for 12 minutes. Meanwhile, wave- or oscillation-like patterns occur four times at the base of the slice L1 covering the LB and adjacent umbra, evidenced by the alternating appearance of the blueshifts and redshifts. The long time interval of the blueshift in the jets possibly indicates that they are not driven by the oscillations. The brightenings in the bright fronts of jets in the AIA 171, 193, and 211 Å channels have some fine structures, manifested as two mini jet-like (marked by the two arrows in Figure 2(f)) brightenings on the background of the jets' fronts near 17:47 UT, together with the brightening wings in the H α line. The interval of the two jets is about 1 minute. Moreover, two similar mini jet-like structures with an interval of about 2 minutes can also be found near 17:23 UT (marked by the two arrows in Figure 2(b)) and are most clearly seen in the 131 Å channel, but they are present in the others. The mini jets in such a short time interval are not possibly caused by the leakage of waves, supporting its correlation with magnetic reconnection. These mini and short-lived jets possibly reveal some fine structures during the magnetic reconnection process.

The line wing enhancement in the H α line occurs not only at the point shown in Figure 2(h), but also at other points on the footpoints of the jets located on the LB. Figure 3 presents the brightenings on the LB observed at -0.8 Å from the H α line center for different stages of the evolution. In Figures 3(a) to (c), they show that the jets move to higher layers, evidenced by the increasing length of the jets along their propagation direction. Note that the footpoints of the jets get bright and look

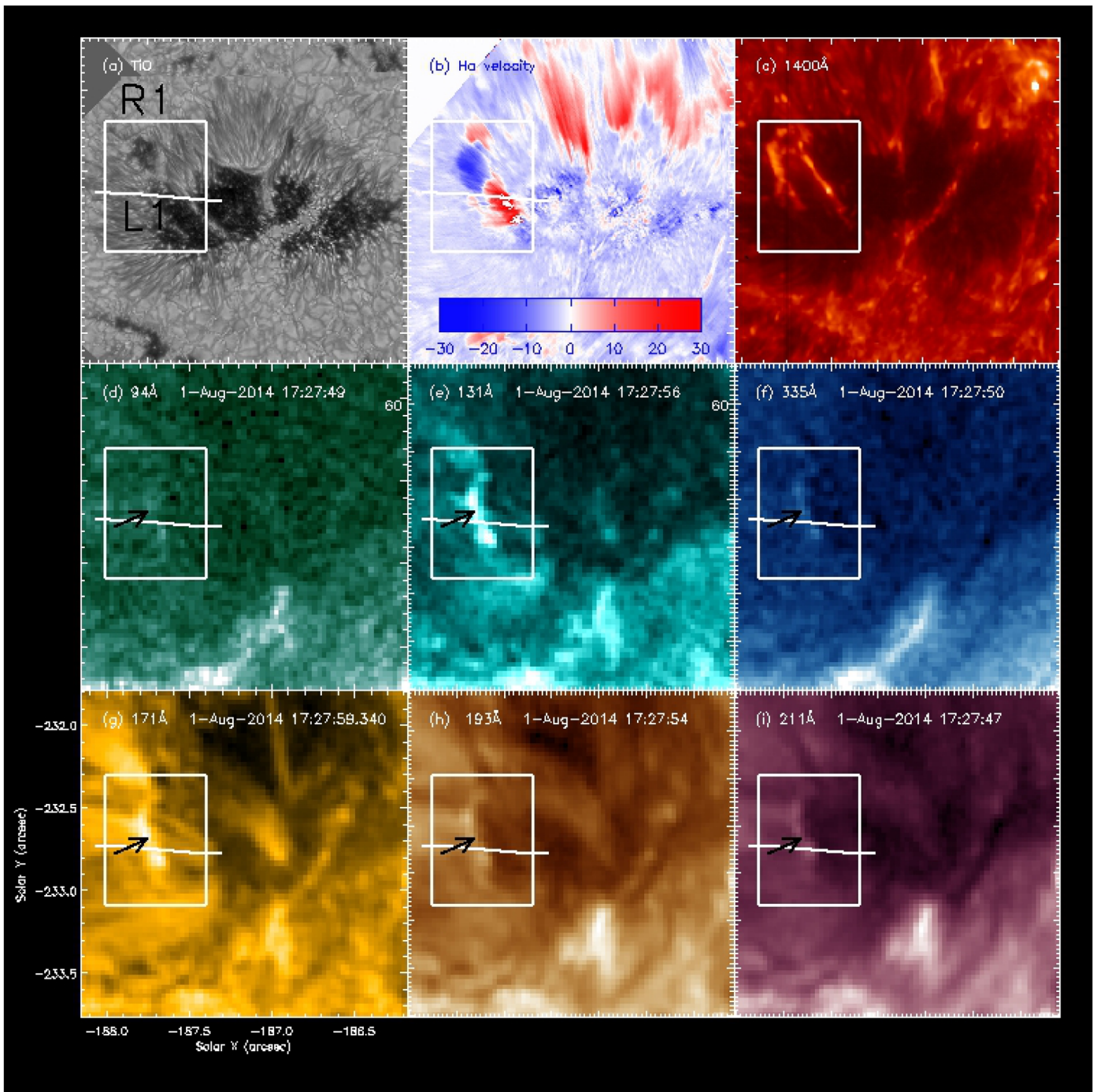


Figure 1. Context images of the LBs and fan-shaped jets on the sunspot of AR 12127 obtained on 2014 August 1 around 17:27 UT. The different panels show (a) the photosphere through TiO images from GST, (b) the chromosphere via Ha LOS velocity obtained with GST/VIS, (c) the TR through SJI 1400 Å images from IRIS, and (d)–(i) the corona response observed with the different filters of SDO/AIA. R1 illustrates the LB region, to be analyzed in Figure 3. L1 represents a slice to be used in Figure 2. The black arrows in panels (d)–(i) mark bright fronts of the fan-shaped jets seen in 171 Å. An associated animation of these nine panels is available online. The animated frames run from 17:15 to 17:55 UT.

(An animation of this figure is available.)

like a ribbon at 17:20:38 UT. From Figures 3(d) to (f), one can find that the ribbon-like brightening propagates along the LB at a speed of about 9.46 km s^{-1} , indicated by the green solid line. Meanwhile, the jets on the LB move in the same direction as the brightenings (marked by the arrows), which is almost perpendicular to the jets' propagation direction. According to Figures 3(g)–(i), the jets occur first at both ends of the LB with remarkable brightenings at their footpoints. Then, the

brightenings at both ends move in opposite directions with a speed of about 30 km s^{-1} . At 17:48:53 UT, one can also see a long ribbon appearing along the entire LB (see the online animation associated with Figure 3). The jets are launched along the entire LB soon afterward. The ribbon motions seem to be the signatures of slipping reconnection, which is generally found in the flare ribbons (Aulanier et al. 2006; Li & Zhang 2014; Li et al. 2016; Jing et al. 2017). The result

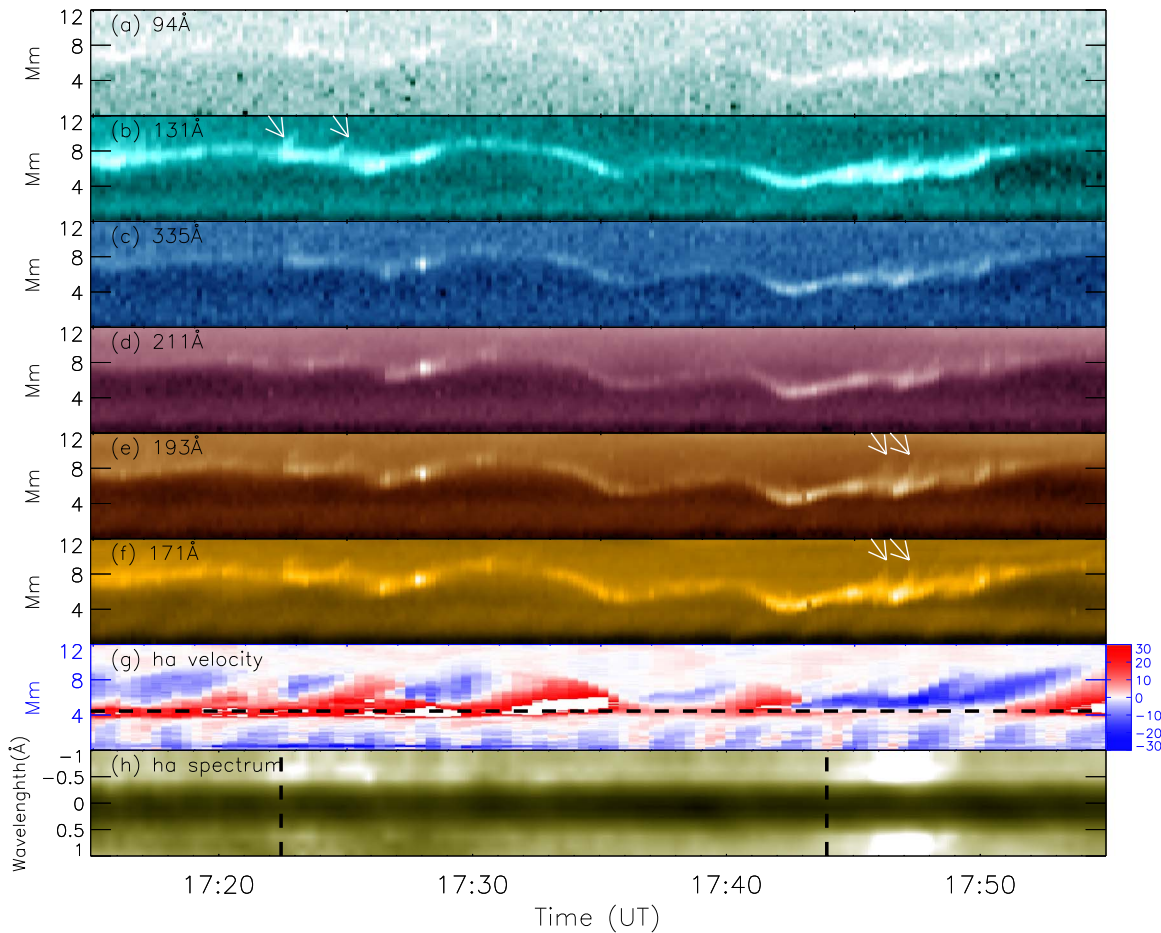


Figure 2. Spacetime map along the slice L1 shown in Figure 1. Panels (a)–(f) show the maps for the different filters of AIA, namely 94, 131, 335, 211, 193, and 171 Å. Panel (g) contains the LOS velocity of the $H\alpha$ line. Panel (h) shows the evolution of the $H\alpha$ spectrum at the location marked by the horizontal dashed line in panel (g). Two white arrows near 17:47 UT mark the two mini jets occurring at a time interval of about 60 s on the bright jet’s front. The two vertical dashed lines in panel (h) mark the two times associated with the $H\alpha$ line wing enhancements and the beginning of blueshifts in the $H\alpha$ LOS velocity.

reveals the three-dimensional nature of the fan-shaped jets. The magnetic reconnection occurs successively at different locations on the LB so that we can see the brightening motions. The width of the ribbon is about $0''.3$, much smaller than the spatial resolution of AIA.

3.2. The TR Spectrum at the Footpoint and Bright Front of the Fan-shaped Jets

In this coordinated campaign, IRIS merely has one scan during the time interval of observations with 64 steps. The upper panels of Figure 4 show the slit scanning image near the line centers of the Si IV 1402.77 Å and Mg II K2v at 2795.94 Å. Similar to the bright features of *SDO/AIA* mentioned above, both the footpoints and the front of the jets are also bright in Si IV 1402.77 Å and Mg II K2v. Note that although Mg II K2v and $H\alpha$ are both chromospheric lines, the latter does not show any bright fronts, possibly due to the increase in source function at the selected wavelength position (Leenaarts et al. 2013). Those brightenings suggest that there is heating of the chromospheric and TR region plasma on the jets.

In order to analyze the IRIS spectral information, we choose three points on the bright fronts of the fan-shaped jets (marked by P1, P2, and P3) and two points on their footpoints

(P4 and P5). Their corresponding spectrum in C II 1335, Si IV 1394, and 1403 Å is shown in the panels in the lower two rows of Figure 4. The black line is the reference spectrum from the average of the bottom rows of the slit scanning image with a region of $12'' \times 2''$. The three points on the jets’ bright fronts show three different types of spectra, and all of them have line broadening relative to the reference spectral profiles, as seen from the Si IV 1403 and 1394 Å lines. The green line, located at the brightest region (P2), has the highest emission. The blue line for P3, whose emission is at the intermediate level, shows a strong blue asymmetry in all of the lines of Si IV 1397, 1403 Å and C II 1335 Å characterized by multicomponent profiles. The red line located at P1 has the weakest emission among the three points and manifests as two Gaussian emission structures, which is an indication of plasma motions with two components. This idea could be supported by the results of Nóbrega-Siverio et al. (2017, 2018). In those papers, the authors show that for surges, the alignment of the LOS with the orientation of the ejections is key to understanding the remarkable TR brightenings as well as the multicomponent profiles. This result for surges could also be applied for our jets, so the multicomponent profiles found may be due to the integration of the multiple-crossing emitting layers of the folded TR on the fan-shaped jets with different LOS velocities.

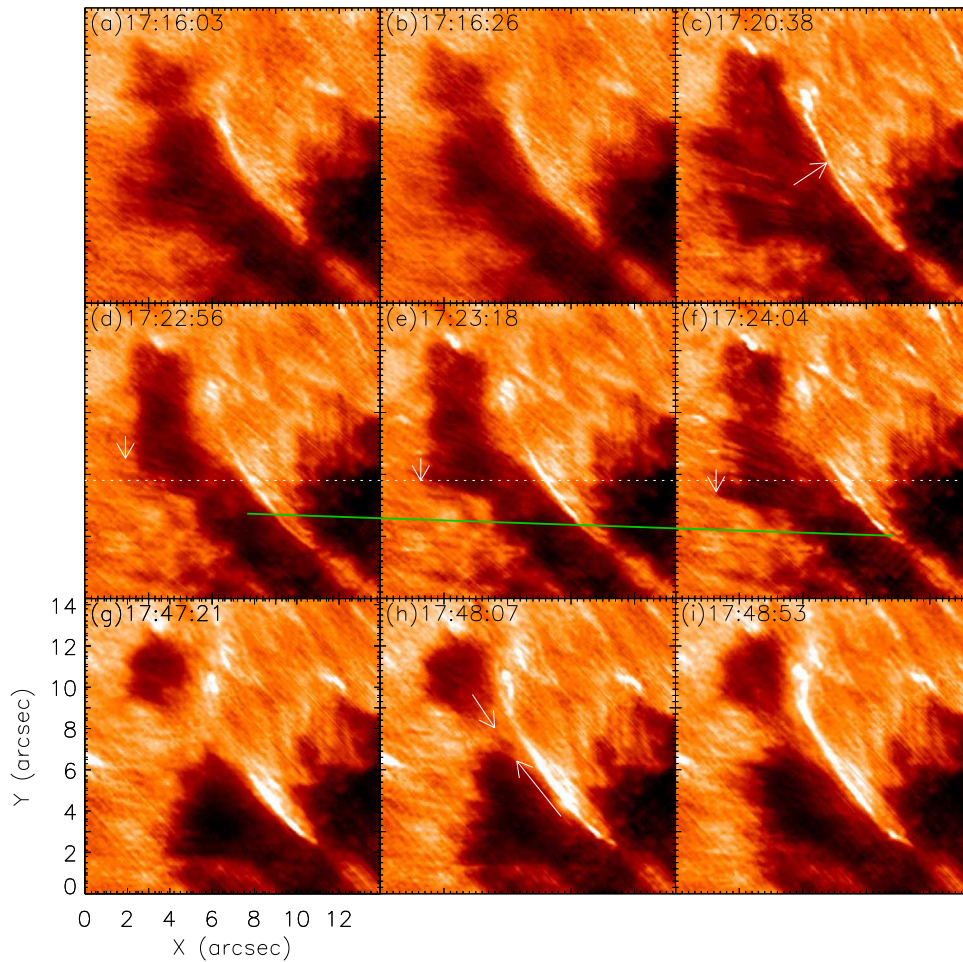


Figure 3. Evolution of the $H\alpha$ off-band images at -0.8 \AA from the line center. The white arrow in panel (c) marks a ribbon-like brightening on LBs, associated with the fan-shaped jets. The green solid line illustrates the brightening motion on LBs along with the jets' motions perpendicular to their moving direction, which is possibly an indication of slipping reconnection. Two opposite arrows in (h) show the moving directions of the brightenings at both ends of the LBs, which finally form a complete ribbon. An associated animation is available online. In the movie, the left panel displays the photospheric images superposed with the contours from the $H\alpha -0.8 \text{ \AA}$ passband images. The blue contours mark the fan-shaped jets, while the red contours mark the brightenings on the LB. The right panel shows the corresponding $H\alpha$ passband images at -0.8 \AA from the line center.

(An animation of this figure is available.)

The footpoints of the fan-shaped jets (P4 and P5 in Figure 4) show line broadening and intensity enhancement. We also find absorption structures of Ne II 1393.33 and 1335.2 \AA superimposed on the lines of Si IV 1393.76 \AA and C II 1335 \AA , especially for P5 (green line) with a higher emission. The appearance of the absorption features in enhanced TR spectral profiles is an indication of a hot reconnection region below the dense and cold plasma (Peter et al. 2014; Tian et al. 2018). We also checked the $H\alpha$ images at -0.8 \AA from the line center and found that there are intermittent intensity enhancements at the same time. These observational characteristics also support the idea that the fan-shaped jets are caused by magnetic reconnection. Note, however, that the absorption features observed here are not akin to the one discussed by Tian et al. (2018). In their paper, significant line broadening of the Si IV, C II, and Mg II h&k lines is found, and the Mg h&k lines show strong absorption due to large opacity. Almost all of the lines have absorption line structures. In our data, no significant absorption structures are found in the Si IV 1403 \AA line, possibly because the emission at P4 and P5 is relatively weaker.

3.3. Photospheric Large-scale and Small-scale Convection Flows on LBs Driving the Magnetic Reconnection

Concerning Hinode/SP data, two scans were performed from 17:15 to 17:55 UT. Figure 5(a) shows the longitudinal magnetic field in level 2 for region R1 as shown in Figure 1(a). It can be found that its value is much lower than that in the pore or umbra. The arrows superimposed on the panel indicate the strength and direction of the transverse magnetic field. The transverse field changes its direction on LB, indicating the existence of magnetic shear. The current sheet is formed at the magnetic shear region, storing enough nonpotential energy for the fan-shaped jets (Toriumi et al. 2015a). We also obtained the inclination angles on the LB and show them in Figure 5(b). The inclination angles, with values close to 90° , are much larger than those in the nearby pores and umbra, revealing an almost horizontal magnetic structure.

We derived the horizontal velocity on the LB with the high-resolution TiO images from GST following the method explained by Liu et al. (2018). The result is arranged in Figures 5(c) and (d), where the corresponding background images are the SP LOS velocity and the TiO image,

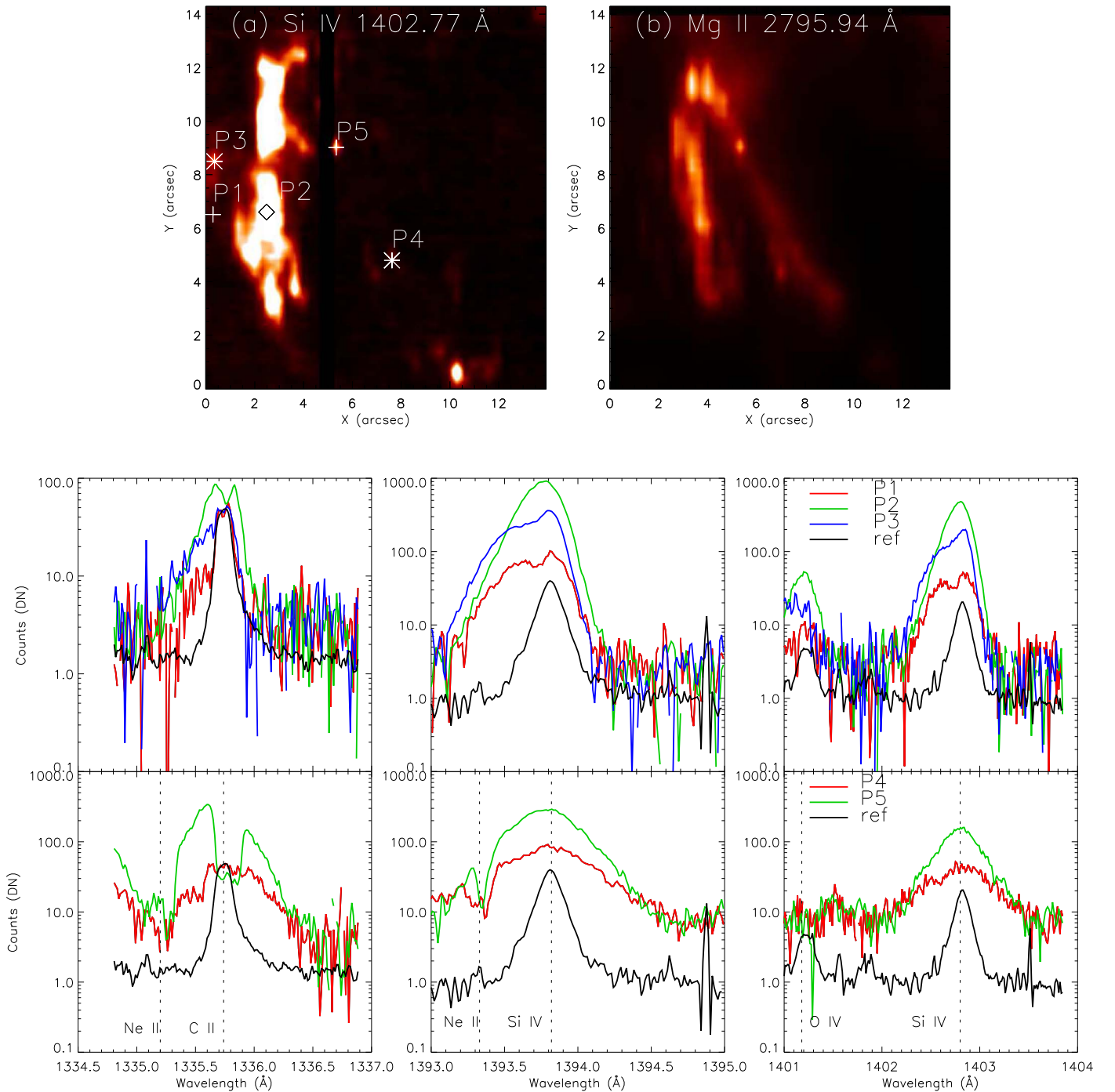


Figure 4. The top row shows the slit scanning maps at the line centers of the Si IV 1402.77 Å and Mg II K2V lines. From left to right in the lower two rows are the spectra extracted from the three points at the bright fronts of jets (upper panel) and the two points at their footpoints (bottom panel) in the lines of C II 1335, Si IV 1394, and 1403 Å, respectively. The black curve is the reference spectrum from the average of a region of $12'' \times 2''$ in the slit scanning image, as shown in the top row of panels.

respectively. The presented horizontal velocity corresponds to the times 17:27 and 17:44 UT. When plotting the horizontal velocity, a running average of the ones calculated from the method of Liu et al. (2018) with a time interval of 100 s is adopted so as to reduce the noise. Two large-scale flow structures occur during the 40 minutes of observation (see the online animation associated with Figure 5). They move in the opposite direction from almost the center of the LB, with the upper left to one end of the LB and that in the lower right to the other end of the LB. The maximum speed of the horizontal

flow is about 1.8 km s^{-1} . From the background image in Figure 5(c), one can also find that the upper left part of the LB has an upflow being blueshifted, while the lower right part has a downflow. In the upper left part (region R2), the plasma on the LB shows an upward motion and changes to downward motions at the boundary between the LBs and the nearby pore, indicating the convective motions of the LBs.

The small-scale photospheric convection on the LB can be found from the evolution of the TiO images in region R2, covering the upper left parts of the LB. The result is shown in

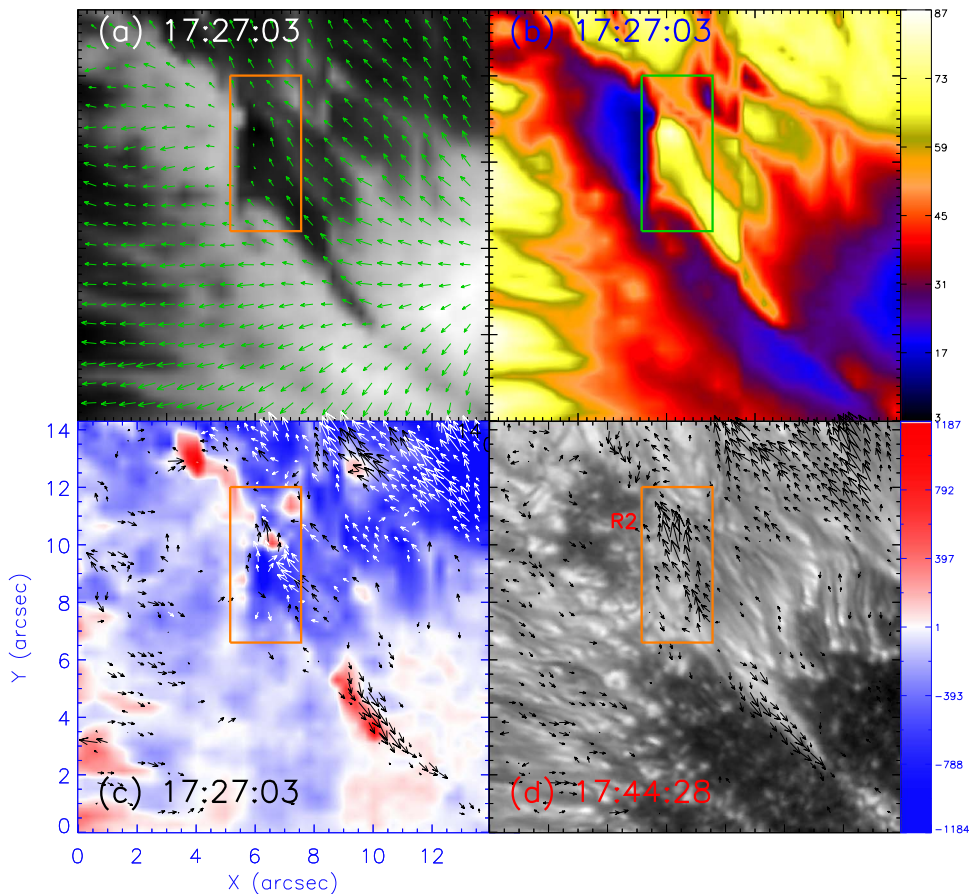


Figure 5. (a) Longitudinal magnetogram in region R1 as shown in Figure 1. The arrow represents the length and direction of the transverse magnetic fields. (b) Inclination angle map. (c) LOS velocity map from the SP data near 17:27 UT. (d) TiO images at 17:44 UT from GST. The arrows in panels (c) and (d) mark the horizontal velocity derived from a series of TiO images. The longest arrow represents 1.8 km s^{-1} . R2 is a selected region to be used in the following figure. An associated animation of the TiO images is available online. The animation has two panels of TiO images, including the horizontal velocity arrows (left panel) and without arrows (right panel).

(An animation of this figure is available.)

Figure 6. From 17:20 to 17:25 UT, one can find some fragmental structures near the location of P6. At time 17:27, they develop into a new convection cell that expands after comparing with the subsequent images. In addition, the direction of horizontal velocity in the region as shown in Figure 5(c) shows that the flow moves from the cell center to its boundary. Combining the upflows in the LOS velocity, it indicates the emergence of a new convection cell. Intensity enhancements at 17:27 UT near P6 on the TiO image are obvious. The red contour marks the brightenings seen from the simultaneous $\text{H}\alpha -0.8 \text{ \AA}$ passband. It indicates that there is a response in the photosphere during the EBs, probably related to the magnetic reconnection heating. From 17:40 to 17:51 UT, the motion of a dark lane (marked by the arrow) is notable. It first occurs near the boundary of the penumbra and the LB, then moves to the upper left direction, and finally reaches the upper boundary of the LB. At the times 17:49 and 17:51 UT, one can also find intensity enhancements near the dark lane on the TiO images, which are accompanied by the brightenings in the $\text{H}\alpha -0.8 \text{ \AA}$ passband. The scenario shows that the small-scale photospheric convection plays an important role in triggering the EBs and subsequent fan-shaped jets. Recently, Pasechnik (2018) also reported an increase in the core intensity of the studied photospheric lines, correlated spatially with the enhanced emission in the $\text{H}\alpha$ line wing.

3.4. Abnormal Stokes V Profiles on LBs Associated with the $\text{H}\alpha$ Line Wing Brightenings

From the SP longitudinal magnetograms in level 2, we did not find small-scale magnetic structures with opposite polarity on the LB. However, abnormal Stokes V profiles do exist in the level 1 data. The locations of the abnormal Stokes V profiles are marked by P6 and P7 in Figure 6. The corresponding Stokes I, Q, U, and V profiles can be found in Figure 7, acquired at 17:27 and 17:44 UT, respectively. Note that there is an enhanced emission at the $\text{H}\alpha -0.8 \text{ \AA}$ passband near the two times, possibly indicating the line wing brightening has a close connection with these abnormal Stokes V profiles. The asymmetry in the red wings of Stokes I profiles is obvious in Figure 7. The abnormal Stokes V profiles have three lobes, which is an indicator of the complexity of the LB magnetic field configuration. Taking a look at the TiO images, we can find that there are fine structures in both the P6 and P7 regions, pointing again to the highly complex LB environment. Similar abnormal Stokes V profiles have also been found in the penumbra (Bellot Rubio et al. 2004; Ruiz Cobo & Asensio Ramos 2013; Lagg et al. 2014; Franz et al. 2016), which is thought to be the indication of returning magnetic flux. Louis et al. (2014) and Felipe et al. (2017) also reported the Stokes V profiles with multiple lobes on the LBs. The three lobes in

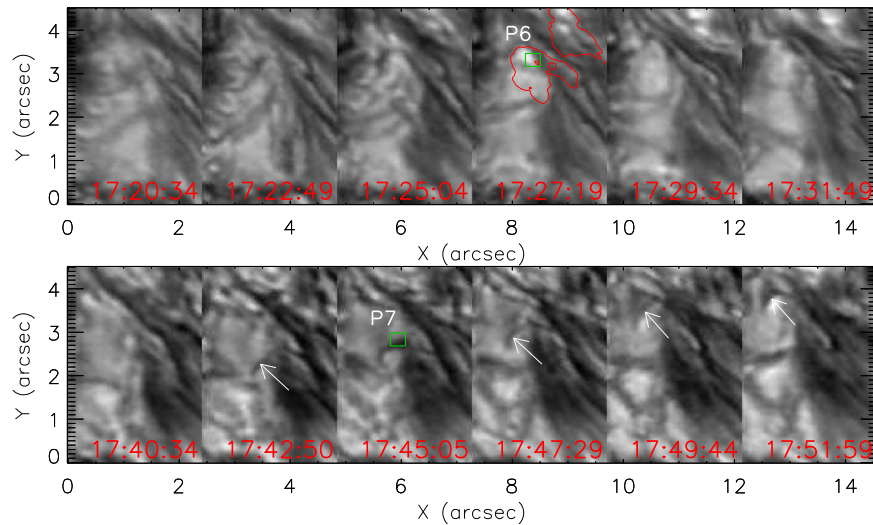


Figure 6. Evolution of the TiO images in R2, the rectangular region shown in Figure 5. The red contours in the upper row mark the regions where we see brightenings in the $H\alpha -0.8 \text{ \AA}$ passband image. P6 and P7 are the locations where the abnormal Stokes V profiles are found. Those two locations have the same size as two pixels of Hinode/SP, and their corresponding Stokes profiles are shown in Figure 7. White arrows in the bottom row mark the positions of a dark lane in fast motion.

Stokes V profiles are generally interpreted as the signature of opposite polarity in the LOS direction.

In order to fit the observed Stokes I, Q, U, and V profiles, we employ the NICOLE code (Socas-Navarro et al. 2015), which is very powerful in dealing with these abnormal profiles thanks to its flexibility in accommodating complex atmospheric models. The level 2 data of Hinode/SP are generated with the analytical solution of the polarized radiative transfer equation under the assumption of a MilneEddington atmosphere model, which is unable to generate the asymmetric profiles. The solid lines in Figure 7 are the best-fitting results. In total, eight nodes in the temperature, four nodes in the LOS bz, and four nodes in the LOS velocity are used in the inversion. The LOS b_x and b_y have one node. NICOLE can reproduce most of the observing profiles, especially the three lobes in Stokes V profiles. We present the atmospheric parameters output from NICOLE in Figure 8.

The error bars in the figure have been computed with a Monte Carlo approach, by performing many inversions with different initializations. The errors reflect the statistical spread of the solutions that converged to a fit of quality similar to the best inversion. This approach is optimal for studying the uncertainties due to line sensitivity or possible ambiguities in the solution (possible uniqueness issues); it is constrained to the specific model scenario chosen in this work. For example, it does not rule out other possible solutions obtained with a larger number of nodes or a more complex scenario.

The fitted temperature at P6 covering the enhanced emission in the TiO images also shows a temperature enhancement near the height of 250 km, reconfirming the above conclusion that the photosphere is disturbed during the EBs. The temperature at P7 also has a temperature enhancement, but the value is about 500 K lower than that at P6. From the lower panel in Figure 6, P7 contains the dark lane and its nearby convective cells with higher emission. The fitted temperature at P7 possibly indicates the hot (the temperature enhancements) and cool (dark lane) components. The b_x and b_y are 0 and 600 G at P6, while their values are 320 and -800 G at P7, respectively. The key point in generating the three lobes in the Stokes V profiles is to add stratification with height for the bz and LOS velocity. The bz in

the low height has a negative value, while it changes to positive values in the upper height. The scenario reveals that there are mixed polarities at P6 and P7. Regarding the LOS velocity, it manifests as redshift in low height while being near zero in the upper height. The redshift (downflow) corresponds to negative polarity, contrary to the adjacent magnetic fields. The scenario is possibly consistent with the result from Lagg et al. (2014), who show that the downflowing material at the boundary of the LB is able to drag down magnetic field lines, creating a region where additional heating might occur. Felipe et al. (2016) also claimed that the LBs are in a plasma-dominated region with a plasma β larger than 1, and the convective flow observed on the LBs is able to bend the magnetic field lines to produce field reversals.

4. Summary and Discussion

The joint observations of fan-shaped jets on a light bridge in the decay phase of AR 12127 give us an excellent opportunity to investigate their dynamic behavior in detail. Part of our results are consistent with previous reports. For example, fan-shaped jets have bright fronts and intermittent brightenings at the footpoints. The emission of the TR lines has line broadening and intensity enhancements. The appearance of the Ne II absorption feature is superimposed on the Si IV 1393.76 \AA and C II 1335 \AA lines at the footpoints of the jets. Furthermore, the present work shows some new observational characteristics, which are summarized as follows:

1. The brightest intensity on the front of jets seen in the AIA EUV channel is accompanied by the initiation of upward motion from the $H\alpha$ LOS velocity. Around the same time, the $H\alpha$ line wings show intensity enhancements, while those at the line center are not obvious, being an indication of EBs. One of the jets shows a continuous upward motion lasting for 12 minutes. On top of the bright jets' fronts, two small-scale jet-like structures also exist with a very short lifetime and a time interval as short as 60 s. These results support the idea that the fan-shaped jets are caused by magnetic reconnection, especially for the occurrence of the small-scale jets.

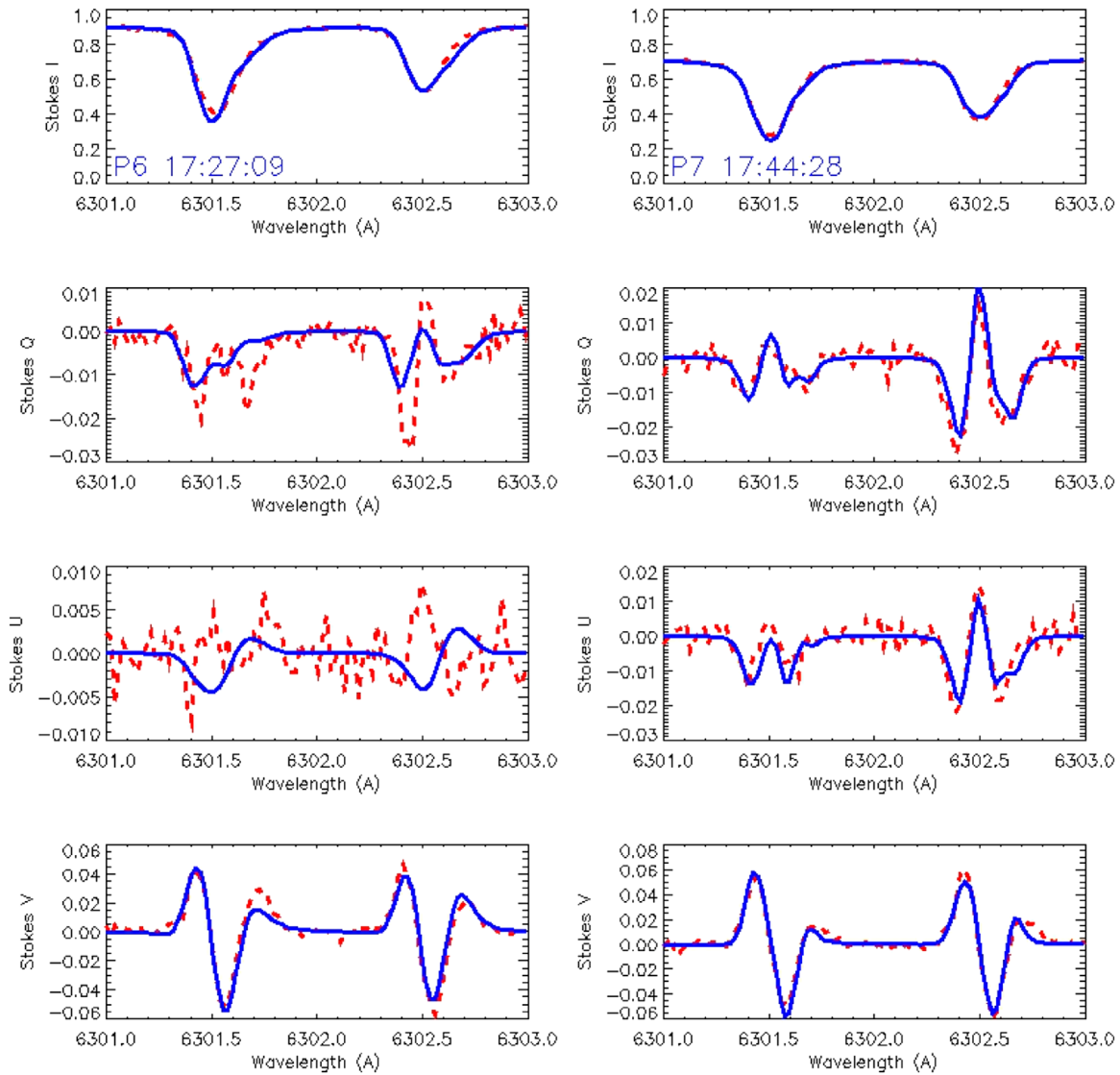


Figure 7. Stokes I, Q, U, and V profiles in the two locations shown in Figure 6: P6 (left column) and P7 (right column). The red dashed lines are the observational profiles from Hinode/SP, while the blue curves are the fitting results obtained using the NICOLE code.

2. Ribbon-like brightenings are found at the footpoints of the LB in the $H\alpha -0.8 \text{ \AA}$ passband images. They also move along the LB, probably showing the scenario of slipping reconnection. This reflects the three-dimensional nature of the fan-shaped jets. In addition, the two-component profiles in the Si IV 1403 and 1393 \AA lines at the bright jets' fronts confirmed the multiple-crossing effect from the simulation of Nóbrega-Siverio et al. (2017, 2018).
3. There are continuous large-scale motions on the LB. The LOS velocities are opposite along the LB, similar to the Evershed flow. Parts of the horizontal flows are to one end of the LB (its nearby umbra), while the other flows are moving to the other end (the pore structures) in the opposite direction. Besides the large-scale motions, small-scale motions also exist, as presented in Figure 6. Evolution of the TiO images shows two kinds of convective motions. One seems to be the emergence of a new convective cell that is evidenced by the low-resolution blueshift and the horizontal divergency flows. The other manifests as a dark lane passing through the

convection cells of the LB. The dark lane is formed at the boundary of the LB and its nearby penumbra. We are not sure whether it is a moving magnetic structure, due to the lack of magnetograms with high spatial and temporal resolution. Line wing brightenings are found in the $H\alpha$ line associated with these photospheric motions, indicating that the convection motions at the photosphere play important roles in generating the fan-shaped jets on the LB.

4. The level 1 data with a fast mode from Hinode/SP show abnormal line profiles on the LB, that is, three lobes in the Stokes V profiles and red asymmetry in the Stokes I profiles. Employing the NICOLE code, we are able to reproduce these profiles, which are likely produced by mixed polarities and a velocity gradient along the LOS direction. The location of the abnormal Stokes profiles is near the boundary of the LB, where the configuration of magnetic fields is very complicated. The convective motions in the convection cells are possibly able to carry some small-scale magnetic fields out to the edge of the LB and interact with the preexisting sunspot magnetic

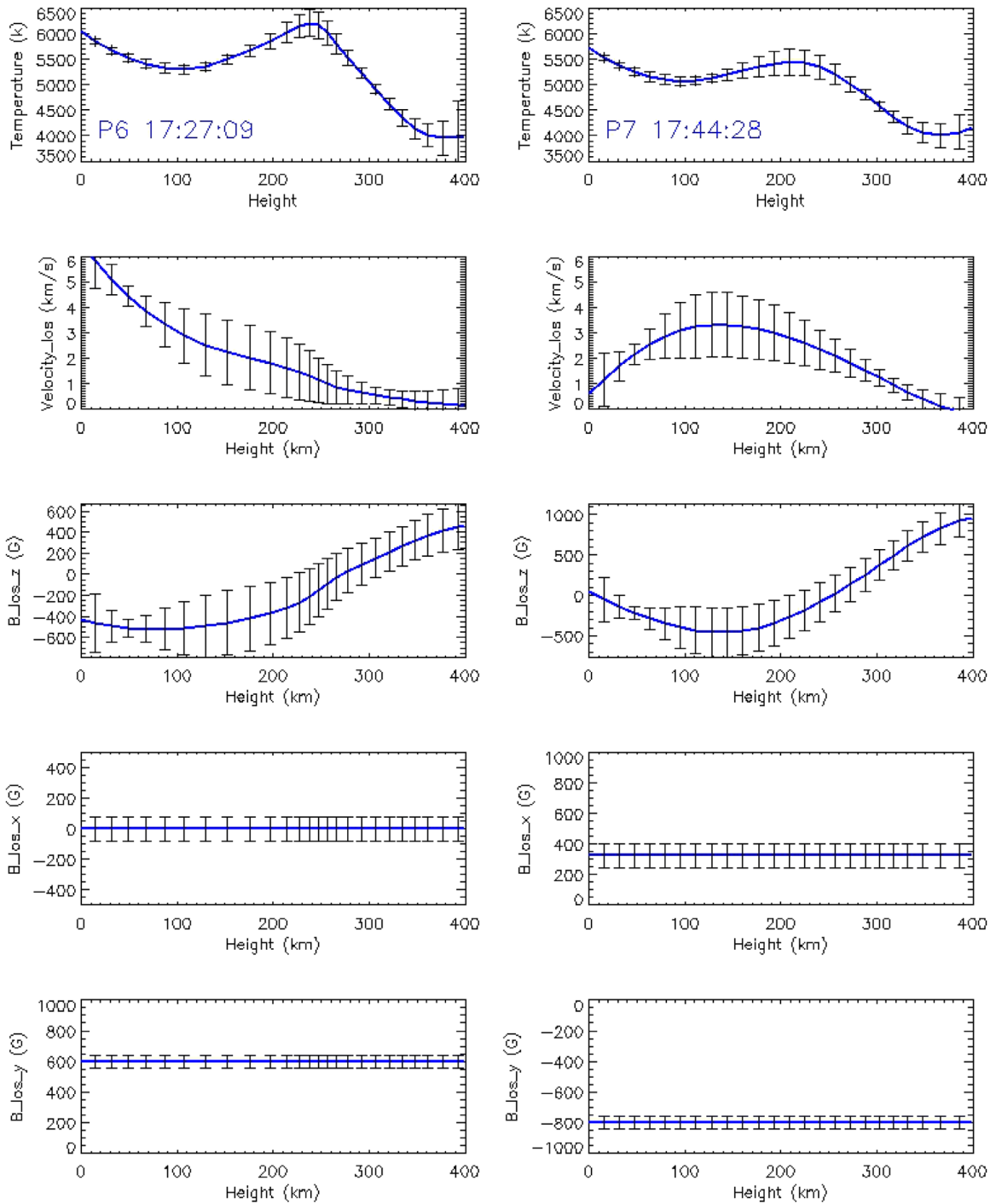


Figure 8. Output model and corresponding estimated error obtained with the NICOLE code for the regions P6 (left column) and P7 (right column). From top to bottom is shown the stratification with height of temperature, LOS velocity, and the LOS of the three components of the magnetic field, namely, B_z , B_x , and B_y .

fields, causing the magnetic reconnection. However, due to the limited resolution of the Hinode/SP, it is difficult to find direct evidence of the opposing polarities in the convection cells of the LB. With the high spatial and temporal resolution vector magnetograms of GST, it is possible to find more evidence of the magnetic fields with mixed polarities.

Combining the small-scale photospheric motion, the abnormal Stokes profiles, the appearance of mini jets with a short interval on the bright jets' fronts in the AIA channels, the $H\alpha$

line wing enhancements, the motions of ribbon-like brightenings at the $H\alpha - 0.8 \text{ \AA}$ passband, and the Ne II absorption feature in the TR lines, we claim that the fan-shaped jets on the LB are due to magnetic reconnection at the upper photosphere or lower chromosphere.

The length of the fan-shaped jets analyzed here is about 4 Mm, in the range of the classification of the jets caused by magnetic reconnection from Tian et al. (2018). Numerical simulations are indeed a powerful tool for understanding the fan-shaped jet activities on LB. Unfortunately, the simulation from Toriumi et al. (2015a) of an emerging LB does not

contain the upper solar atmosphere, so it is not able to investigate the dynamics of the jets and the physical mechanisms behind them. Nóbrega-Siverio et al. (2016, 2017) carried out 2.5D numerical experiments in which a surge results from magnetic flux emergence; the simulation contains the photosphere, chromosphere, TR, and corona. The results from their simulation can explain some of the observations in the paper. But the simulation is not carried out in terms of LBs. Also due to its 2.5D nature, it cannot recover all of the observations in the paper, especially in the transverse motions of the jets and the ribbon-like brightenings seen in Figure 3. More work needs to be done on the simulation of fan-shaped jets on LBs, and our results can provide some useful information to constrain the physical parameters of the simulation.

We thank the BBSO's observing and engineering staff for support and observations. The BBSO operation is supported by NJIT and an NSF AGS-1821294 grant. The GST operation is partly supported by the Korea Astronomy and Space Science Institute and Seoul National University and by the strategic priority research program of the Chinese Academy of Science (CAS) with grant XDB09000000. We acknowledge the free data usage policy of the *SDO*. IRIS is a NASA small explorer mission developed and operated by LMSAL with mission operations executed at NASA Ames Research Center and major contributions to downlink communications funded by ESA and the Norwegian Space Centre. We also thank the Community Spectropolarimetric Analysis Center for providing the HINODE/SP data. This research work is supported by grants 11873062, 11427901, 11427803, 11773072, 11773038, 11773040, 11703042, U1731241, 11573012, 11673038, XDA15010800, XDB09040200, and U.S. NSF AGS-1821294. The work is also supported by a Young Researcher Grant from the National Astronomical Observatories, Chinese Academy of Sciences. This research work is supported by grant No. 11873062, 11427901, 11427803, 11773072, 11773038, 11773040, 11703042, U1731241, 11573012, 11673038, XDA15010800, XDB09040200, U.S. NSF AGS-1821294 and by a Young Researcher Grant from the National Astronomical Observatories, Chinese Academy of Sciences. This research was also supported by the Research Council of Norway through its Centres of Excellence scheme, project No. 262622, and through grants of computing time from the Programme for Supercomputing.

ORCID iDs

Hector Socas-Navarro  <https://orcid.org/0000-0001-9896-4622>

Daniel Nóbrega-Siverio  <https://orcid.org/0000-0002-7788-6482>

Dong Li  <https://orcid.org/0000-0002-4538-9350>

References

Asai, A., Ishii, T. T., & Kurokawa, H. 2001, *ApJL*, 555, L65
 Aulanier, G., Pariat, E., Démoulin, P., & DeVore, C. R. 2006, *SoPh*, 238, 347
 Bellot Rubio, L. R., Balthasar, H., & Collados, M. 2004, *A&A*, 427, 319
 Berger, T. E., & Berdyugina, S. V. 2003, *ApJL*, 589, L117

Bharti, L. 2015, *MNRAS*, 452, L16
 Bharti, L., Rimmele, T., Jain, R., Jaaffrey, S. N. A., & Smartt, R. N. 2007, *MNRAS*, 376, 1291
 Cao, W., Gorceix, N., Coulter, R., et al. 2010, *AN*, 331, 636
 Chen, Y., Tian, H., Xu, Z., et al. 2017, *GSL*, 4, 30
 Cheung, M. C. M., Rempel, M., Title, A. M., & Schüssler, M. 2010, *ApJ*, 720, 233
 De Pontieu, B., Title, A. M., Lemen, J. R., et al. 2014, *SoPh*, 289, 2733
 Ellerman, F. 1917, *ApJ*, 46, 298
 Felipe, T., Collados, M., Khomenko, E., et al. 2016, *A&A*, 596, A59
 Felipe, T., Collados, M., Khomenko, E., et al. 2017, *A&A*, 608, A97
 Franz, M., Collados, M., Bethge, C., et al. 2016, *A&A*, 596, A4
 Hong, J., Carlsson, M., & Ding, M. D. 2017a, *ApJ*, 845, 144
 Hong, J., Ding, M. D., & Cao, W. 2017b, *ApJ*, 838, 101
 Hou, Y., Zhang, J., Li, T., Yang, S., & Li, X. 2017, *ApJL*, 848, L9
 Hou, Y., Zhang, J., Li, T., et al. 2016a, *ApJL*, 829, L29
 Hou, Y. J., Li, T., Yang, S. H., & Zhang, J. 2016b, *A&A*, 589, L7
 Jing, J., Liu, R., Cheung, M. C. M., et al. 2017, *ApJL*, 842, L18
 Jurčák, J., Martínez Pillet, V., & Sobotka, M. 2006, *A&A*, 453, 1079
 Katsukawa, Y., Yokoyama, T., Berger, T. E., et al. 2007, *PASJ*, 59, S577
 Lagg, A., Solanki, S. K., van Noort, M., & Danilovic, S. 2014, *A&A*, 568, A60
 Leenaarts, J., Pereira, T. M. D., Carlsson, M., Uitenbroek, H., & De Pontieu, B. 2013, *ApJ*, 772, 89
 Leka, K. D. 1997, *ApJ*, 484, 900
 Lemen, J. R., Title, A. M., Akin, D. J., et al. 2012, *SoPh*, 275, 17
 Li, T., Yang, K., Hou, Y., & Zhang, J. 2016, *ApJ*, 830, 152
 Li, T., & Zhang, J. 2014, *ApJL*, 791, L13
 Lites, B. W., Akin, D. L., Card, G., et al. 2013, *SoPh*, 283, 579
 Liu, H., Yang, Y. F., Shang, Z. H., & Li, H. X. 2018, *AR&T*, 15, 151
 Liu, S. 2012, *PASA*, 29, 193
 Liu, S., & Liu, D. 2015, *AdSpR*, 55, 2931
 Louis, R. E., Beck, C., & Ichimoto, K. 2014, *A&A*, 567, A96
 Louis, R. E., Bellot Rubio, L. R., de la Cruz Rodríguez, J., Socas-Navarro, H., & Ortiz, A. 2015, *A&A*, 584, A1
 Louis, R. E., Bellot Rubio, L. R., Mathew, S. K., & Venkatakrishnan, P. 2009, *ApJL*, 704, L29
 Nóbrega-Siverio, D., Martínez-Sykora, J., Moreno-Insertis, F., & Rouppe van der Voort, L. 2017, *ApJ*, 850, 153
 Nóbrega-Siverio, D., Moreno-Insertis, F., & Martínez-Sykora, J. 2016, *ApJ*, 822, 18
 Nóbrega-Siverio, D., Moreno-Insertis, F., & Martínez-Sykora, J. 2018, *ApJ*, 858, 8
 Pasechnik, M. N. 2018, *KPCB*, 34, 68
 Peter, H., Tian, H., Curdt, W., et al. 2014, *Sci*, 346, 1255726
 Rezaei, R. 2018, *A&A*, 609, A73
 Rezaei, R., Bello González, N., & Schlichenmaier, R. 2012, *A&A*, 537, A19
 Rimmele, T. 2008, *ApJ*, 672, 684
 Rimmele, T. R. 1997, *ApJ*, 490, 458
 Robustini, C., Leenaarts, J., de la Cruz Rodríguez, J., & Rouppe van der Voort, L. 2016, *A&A*, 590, A57
 Rouppe van der Voort, L., Bellot Rubio, L. R., & Ortiz, A. 2010, *ApJL*, 718, L78
 Roy, J. R. 1973, *SoPh*, 28, 95
 Ruiz Cobo, B., & Asensio Ramos, A. 2013, *A&A*, 549, L4
 Schlichenmaier, R., von der Lühe, O., Hoch, S., et al. 2016, *A&A*, 596, A7
 Shimizu, T., Katsukawa, Y., Kubo, M., et al. 2009, *ApJL*, 696, L66
 Sobotka, M., Bonet, J. A., & Vazquez, M. 1993, *ApJ*, 415, 832
 Sobotka, M., Bonet, J. A., & Vazquez, M. 1994, *ApJ*, 426, 404
 Sobotka, M., & Puschmann, K. G. 2009, *A&A*, 504, 575
 Socas-Navarro, H., de la Cruz Rodríguez, J., Asensio Ramos, A., Trujillo Bueno, J., & Ruiz Cobo, B. 2015, *A&A*, 577, A7
 Song, D., Chae, J., Yurchyshyn, V., et al. 2017, *ApJ*, 835, 240
 Tian, H., Kleint, L., Peter, H., et al. 2014, *ApJL*, 790, L29
 Tian, H., Yurchyshyn, V., Peter, H., et al. 2018, *ApJ*, 854, 92
 Toriumi, S., Cheung, M. C. M., & Katsukawa, Y. 2015a, *ApJ*, 811, 138
 Toriumi, S., Katsukawa, Y., & Cheung, M. C. M. 2015b, *ApJ*, 811, 137
 Vazquez, M. 1973, *SoPh*, 31, 377
 Wöger, F., & von der Lühe, O. 2007, *ApOpt*, 46, 8015
 Yang, S., Zhang, J., & Erdélyi, R. 2016, *ApJL*, 833, L18
 Yang, S., Zhang, J., Erdélyi, R., et al. 2017, *ApJL*, 843, L15
 Yang, S., Zhang, J., Jiang, F., & Xiang, Y. 2015, *ApJL*, 804, L27
 Yuan, D., & Walsh, R. W. 2016, *A&A*, 594, A101
 Zhang, J., Tian, H., He, J., & Wang, L. 2017, *ApJ*, 838, 2